Summer precipitation variability over South America on long and short intraseasonal timescales

Article

Accepted Version

Summer precipitation variability over South America on long and short intraseasonal timescales

Paula L. M. Gonzalez [1], **Carolina S. Vera** [2]

1. International Research Institute for Climate and Society, Columbia University

61 Route 9W, 202b Monell, Palisades, NY 10964 USA

Tel.: +1-845-6804525 / Fax: +1-845-6804865

E-mail: gonzalez@iri.columbia.edu

2. Centro de Investigaciones del Mar y la Atmosfera (CIMA/CONICET-UBA), DCAO/FCEN, UMI IFAECI/CNRS

2[do] piso, Pabellon II, Ciudad Universitaria, 1428, Buenos Aires, Argentina.

Tel.: +54-11-4787-2693/ Fax: +54-11-4788-3592

E-mail: carolina@cima.fcen.uba.ar

ABSTRACT

A dipole pattern in convection between the South Atlantic Convergence Zone and the subtropical plains of southeastern South America characterizes summer intraseasonal variability over the region. The dipole pattern presents two main bands of temporal variability, with periods between 10 and 30 days, and 30 and 90 days; each influenced by different large-scale dynamical forcings. The dipole activity on the 30-90-day band is related to an eastward traveling wavenumber-1 structure in both OLR and circulation anomalies in the tropics, similar to that associated with the Madden-Julian Oscillation. The dipole is also related to a teleconnection pattern extended along the South Pacific between Australia and South America. Conversely, the dipole activity on the 10-30-day band does not seem to be associated with tropical convection anomalies. The

corresponding circulation anomalies exhibit, in the extratropics, the structure of Rossby-like wave trains, although their sources are not completely clear.

Keywords summer precipitation, intraseasonal variability, South America, SASS, MJO

1. Introduction

The most distinctive feature of summer rainfall variability on intraseasonal timescales over South America (SA) is a dipolar pattern known as South American Seesaw (SASS) (e.g.; Casarin and Kousky 1986; Nogues-Paegle and Mo 1997; Diaz and Aceituno 2003). SASS exhibits centers of action of opposite sign in both the South Atlantic convergence zone (SACZ) and southeastern South America (SESA) regions. The phase with enhanced precipitation over the subtropics and a weak SACZ – hereafter `positive phase' - is associated with increased southward moisture flux from the Amazon region to SESA, favored by the presence of a low-level jet to the east of the Andes (Nogues-Paegle and Mo 1997). In the opposite phase, a SACZ enhancement is accompanied by imcreased southeast moisture fluxes from the Amazon region to SACZ and decreased rainfall at the subtropical plains – hereafter `negative phase'. It has been shown that in both phases, the region with enhanced precipitation is more likely to experience extreme rainfall events (e.g.; Carvalho et al. 2004; Liebmann et al. 2004; Gonzalez et al. 2008). Furthermore, Cerne et al. (2007) and Cerne and Vera (2011) showed that during the phase of enhanced SACZ (negative phase of SASS), the associated subsidence promotes a larger frequency of heat waves and extreme heat events over the subtropical center, evidencing that SASS influence is not only restricted to convection and precipitation.

Previous works suggest that SASS is not only a regional feature but also part of a large-scale system (e.g.; Nogues-Paegle and Mo 1997). In particular, Kalnay et al. (1986) and Grimm and Silva Dias (1995) first detected interactions between the SACZ and the South Pacific convergence zone (SPCZ, Vincent 1994) on intraseasonal timescales. Subsequent studies have suggested that the development of Rossby wave trains, forced by the tropical convective activity of the Madden-Julian Oscillation (MJO), influences intraseasonal variability over SA. This interaction between tropics and extratropics is frequently linked to the development of Pacific-South America (PSA) teleconnection patterns (e.g.; Mo and Higgins 1998), as is also observed on interannual timescales (e.g.; Mo and Nogues-Paegle 2001). Li and Le Treut (1999) showed that in winter as well as in summer, a certain phase of the PSA patterns on intraseasonal timescales may induce changes in the moisture transport channeled by the Andes from the Amazon region towards SESA. In addition, Cunningham and Cavalcanti (2006) identified two modes of intraseasonal variability affecting the SACZ, both with timescales between 30 and 60 days. The first mode represents the tropics-tropics interactions and is characterized by a northward displacement of the SACZ with respect to its climatological position. The second mode is related to the tropics-extratropics interactions and is associated with PSA-like patterns.

Nonetheless, SASS activity is not only restricted to the 30-60 day band. Liebmann et al. (1999) showed that OLR intraseasonal variability over the SACZ and the Amazon basin exhibits the most relevant spectral peaks at approximately 48, 27, and 16 days. Consistently, through a singular spectrum analysis, Nogues-Paegle et al. (2000) isolated two main oscillatory modes associated with the SASS Index: one mode with longer periods of variability, between 36 and 40 days (*mode 40*) ; and the other mode with shorter periods, between 22 and 28 days (*mode 20*). OLR anomalies related to mode 20 seem to be more relevant over SESA than those associated with mode 40, while both modes interfere constructively in the negative phase of SASS (Nogues-Paegle et al. 2000). While mode 40 variability has been linked to MJO activity, the sources of that associated with mode 20 remain unclear.

The existent bibliography reveals a special interest on the study of the influence of MJO on South American climate, mainly motivated by the fact that MJO is the only intraseasonal oscillation with a demonstrated degree of predictability (e.g.; Ferranti et al. 1990; Waliser et al. 2003). Nevertheless, different studies have shown that state-of-the-art CGCMs are still deficient at representing the MJO activity (e.g.; Slingo et al. 1996) and consequently its influence on precipitation over SA (e.g.; Lin et al. 2006). Consequently, a profound understanding of such influence together with an improvement in its representation in GCMs could potentially extend the predictability of summer precipitation over SA (Nogues-Paegle et al. 1997; Jones and Schemm 2000; Cavalcanti and Castro 2003; Cunningham and Cavalcanti 2006). In addition, since MJO only explains a small percentage of intraseasonal variability in both subtropical and tropical regions, a more profound understanding of other sources of such variability over SA is also needed.

The objective of this paper is to further explore the physical mechanisms that explain SASS activity on both short (10-30 days) and long (30-90 days) intraseasonal time scales. The work focuses on better understanding the remote forcings of variability in each activity band separately, and to assess whether they act through different dynamical mechanisms. In turn, these results could be useful to identify the strengths and weaknesses of the representation of intraseasonal variability in state-of-the-art general circulation models and to exploit the potential predictability of these processes.

2. Data and methodology

The NOAA interpolated OLR dataset (Liebmann and Smith 1996) over the 1979-2007 period (28 warm seasons) was considered to describe intraseasonal variability of convection over SA. The warm season was represented by the November-March (151 days) period. Filtered OLR (FOLR) anomalies were calculated through a Lanczos band-pass filter (Duchon 1979) for both bands: 10-30 days (hereafter FOLR 10-30) and 30-90 days (hereafter FOLR 30-90).

The leading patterns of variability were isolated for both activity bands, performing two separate Empirical Orthogonal Functions (EOF) analyses of the corresponding FOLR anomalies over SA. In both cases, as it is discussed in the next section, the leading patterns resemble the spatial features associated with SASS. The corresponding standardized principal component time series are considered as the SASS indexes. It is worth mentioning that the methodology used in this work to isolate the leading patterns for the two temporal bands is different from that used in previous studies. For example, Nogues-Paegle et al. (2000) performed first an EOF analysis of the FOLR anomalies representing the full range of intraseasonal timescales (10-90 days) and then they discriminated the SASS signal in both intraseasonal bands through a singular spectrum analysis. In this work we chose to isolate first the FOLR anomalies associated with each temporal band, and then performed the EOF analyses to identify the corresponding SASS patterns (hereafter called SASS 10-30 and SASS 30-90, respectively). This approach was motivated by several points: the fact that MJO concentrates its activity on the 30-90 day band; the previous works that showed the relevance of SASS in both variability bands; and the limitations of an EOF analysis performed in S-mode (which is the usual way of applying EOF), which might not be an appropriate tool to discriminate variability patterns with different dominant timescales (e.g.; Bjornsson and Venegas 1997).

Lagged daily regression maps of FOLR fields were computed using the SASS indexes as reference time series. Lagged regression maps were also constructed for streamfunction zonal anomalies at sigma level $\sigma = 0.2101$, available from NCEP/NCAR Reanalysis (Kalnay et al. 1996). Stastistically significant regression values were identified through a two-tailed Student t-test of the corresponding correlation values at a significance level of 0.05.

3. SASS Dynamics

The SASS patterns obtained through the EOF analysis of both FOLR 30-90 and FOLR 10-30 anomalies are displayed in Figure 1. The SASS 30-90 explains 21.8 % of the variance and exhibits two centers of action over the SACZ and SESA regions, as identified in previous works. The loadings are much larger over the SACZ region than over SESA, and both centers exhibit a strong NW-SE orientation (Fig. 1a). On the other hand, the SASS 10-30 explains 14 % of the variance and it also exhibits a dipole-like structure, with loadings over SACZ slightly larger than those over SESA (Fig. 1b). A comparison of the amplitude of the two SASS patterns shows that the two centers of SASS 10-30 are stronger than the corresponding ones of SASS 30-90. In addition, in the case of SASS 30-90, the NW-SE tilt seems to be somewhat weaker, particularly in the SACZ center.

The spectral properties of both SASS patterns obtained from the corresponding SASS indexes are presented in Figure 2. SASS 10-90 exhibits 3 significant activity peaks at around 44, 57 and 35 days. On the other hand, the SASS 10-30 presents peaks at around 15 and 23 days .

3.1 SASS 30-90

The large-scale FOLR 10-90 anomalies related to SASS 30-90 activity are described using regression maps between lags -30 and +30 days (Figure 3). A negative day implies that FOLR anomalies temporarily lead the SASS 30-90 index. Between days -30 and -20, FOLR anomalies over

SA suggest the development of the SACZ, with an expansion of convection towards the equatorial Atlantic. During that time, the Pacific Ocean is characterized by a suppressed SPCZ and inhibited convection over the warm pool. By day -25, the development of a dipolar structure is discernible over SA, consistent with a negative phase of SASS. Inhibited convection over the Maritime Continent (MC) and increased convection over Africa are also evident; a structure that exhibits estward propagation during the following days. Between days -20 and -15, the dipolar structure over SA weakens and by day -10 a positive phase of SASS starts to develop, and peaks on day 0. In agreement, convection over both SACZ and Africa weakens, while it intensifies over the western portion of tropical South Pacific with a NW-SE orientation, consistent with a strengthened SPCZ. Between days 0 and +10, the positive phase of SASS weakens, while enhanced (weakened) convection over the MC-western tropical Pacific (Africa-tropical Indian sector) continues its eastward propagation. In addition, from day +5 onwards, the SPCZ evolves towards an inhibited phase. Between days +10 and +15, SASS transitions to a negative phase. On day +20 the SACZ intensifies, and so does convection over southern Africa, with a NW-SE orientation that could be associated with the so called South Indian convergence zone (SICZ, e.g.; Cook 2000), but shifted to the SW. This SICZ behavior has been identified as an evidence of the interaction between convection in SA and Africa (Cook et al. 2004).

The SASS 30-90 evolution is similar to that described by Nogues-Paegle et al. (2000) for their mode 40. It is also highly consistent at the tropical band with the MJO life cycle (e.g.; Hendon and Salby 1994), characterized by a zonally oriented convection dipole that propagates eastward along the Equator, from the Indian Ocean to the central Pacific. As it has been described before, such convective anomalies tend to dissipate as they approach the eastern Pacific, where sea surface temperatures (SST) become colder. Consistently, the analyzed regression maps do not show any significant eastward propagation of convection anomalies over tropical SA in association with SASS 30-90 evolution. The fact that SASS remains stationary seems to be related to the SACZ, which is anchored to the continent by the convection associated with the South American Monsoon System (e.g.; Kalnay et al. 1986). The study of the lag-by-day regression time series for two grid points located at each SASS dipole centers (Fig. 4) reveals that the evolution of both centers is highly antisymmetrical, completing a full cycle in approximately 40 days.

The large-scale circulation anomalies associated with the SASS 30-90 evolution are described through the analysis of the regression maps of upper-level streamfunction anomalies

(Fig. 5). Zonal means have been removed from the regressed values in order to highlight the zonal assymetries. The regression maps reveal a wavenumber-1 structure in circulation anomalies at the tropical band that propagates eastward during the whole evolution, resembling that observed in the MJO life cycle. In particular, tropical circulation anomalies persist across the dateline, explaining the connection between convection anomalies in the Indian and western Pacific oceans with those over tropical America (Fig. 3). Figure 6 presents the Hovmöller diagrams of streamfunction regressed anomalies along the tropical band. Eastward propagation of the anomalies is clear between the Indian Ocean and southeastern Pacific, while they acquire a more stationary character over SA.

Regression maps also show circulation anomalies organized in wave trains extended along the South Pacific Ocean, and reaching mid- and high-latitudes (Fig. 5). A clear example can be seen between days -15 and day 0, when opposite sign centers alternate from the Indian and western Pacific oceans towards the high latitudes of the Southern Hemisphere, along an arch-shaped trajectory that reaches SA. The development of such wavetrain occurs while tropical convection intensifies over the MC-western equatorial Pacific sector (Fig. 3). As it was mentioned before, these teleconnection patterns are consistent with those described by Nogues-Paegle et al. (2000) for their mode 40 and they are linked to meridionally propagating Rossby waves (Sardeshmukh and Hoskins 1988). They have been identified in the Southern Hemisphere as the PSA patterns, and can be modulated by tropical convection (e.g.; Mo and Higgins 1998; Mo and Nogues-Paegle 2001). In addition, between approximately day -15 and day +5, a quasistationary wavenumber 3 pattern is discernible at high latitudes. In agreement, Mo and Higgins (1998) found that the two leading patterns of circulation anomalies in the South Pacific on intraseasonal timescales resemble PSA-like structure and are in quadrature by each other, with a signature of wavenumber 3 at midlatitudes.

On day 0, it is evident that in association with a SASS 30-90 positive phase the extratropical teleconnection pattern induces cyclonic (anticyclonic) anomalies at extratropical (tropical) SA. That regional circulation anomaly pattern is consistent with wetter than normal conditions in SESA and dryer conditions in the SACZ region. Between days -5 and +5, another arch-shaped wave train structure is evident across the South Atlantic, linking SA with the tropical Indian Ocean. An analysis of similar regression maps computed at different vertical levels reveals that the circulation anomaly structures exhibit equivalent barotropic structures (not shown).

3.2 SASS 10-30

Regressions maps based on the SASS 10-30 Index were calculated between days -18 and +18 and are discussed in this subsection. Regression maps for FOLR anomalies (Fig. 7) do not show statistically significant convective anomalies at the equatorial Indian and Pacific oceans, in opposition to the case of the SASS 30-90 (Fig. 3). It seems then that no significant MJO influence can be identified on SASS 10-30 activity. This result disagrees with that obtained by Nogues-Paegle et al. (2000), in which their mode 22, as well as their mode 40, were linked to tropical convective activity. As it was discussed in section 2, the disagreement could be due to differences in the methodologies applied to isolate the leading spatio-temporal modes of variability.

In general, spatially coherent significant FOLR anomalies are barely discernible outside of SA in the SASS 10-30 cycle. However, a closer inspection reveals that both SICZ and SPCZ exhibit some signs of activity (e.g.; at around day -12), though it is not possible to detect a clear life cycle associated with these convergence zones. Between days -12 and -9, convection anomalies over SA evolve towards a negative phase of SASS. That pattern weakens between days -9 and -6 and the following shift in SASS phase is evident around days -6 and -3, with FOLR anomalies maximizing at day 0. The SASS 10-30 related dipole also shows stationary features, with centers essentially anchored throughout the whole evolution. The day-by-day evolution of the regressed values at two locations representative of the SASS centers (Fig 8) reveals a certain lag in the opposite relationship that both time series exhibit, that is not observed for SASS 30-90 (Fig. 4). In particular, the negative peak of the subtropical center is reached at day -1 while the corresponding positive peak of the SACZ center does it at day 0. This suggests that the timing of SASS 10-30 is dominated by the SACZ center. In addition, the analysis of these time series confirms that the typical length of the SASS 10-30 cycle is approximately 15 days.

Regression maps between the SASS 10-30 index and upper-level streamfunction anomalies (Fig. 9) reveal at around day -15 the development of a teleconnection pattern along the South Pacific Ocean, extended between 30 S and 40 S. As time evolves, circulation anomalies intensify along the South Pacific, while they exhibit a weak eastward propagation. It can also be noted that these wave trains exhibit a higher wavenumber than those identified for SASS 30-90 (Fig. 5). Over

SA, circulation anomalies become more stationary while northward meridional wave propagation is discernible. At around day 0, the large-scale teleconnection pattern induces cyclonic (anticyclonic) circulation anomalies at extratropical (tropical) SA, in association with a positive phase of SASS 10-30 (Fig. 7). In addition, at approximately day +3, teleconnections develop from SA eastward, crossing the South Atlantic and reaching the Indian Ocean. This wave train might be induced by the SACZ enhancement observed between days -12 and -9 (Fig. 7). Grimm and Silva Dias (1995), among others, confirmed through numerical experiments that such teleconnections can develop. The wave structures emanating from SA northwards as well as eastwards have also been identified by Nogues-Paegle et al. (2000) for mode 22, implying that they are robust signals associated with SASS activity on shorter intraseasonal time scales. the vertical structure of these wave trains are equivalent barotropic, as observed for the long intraseasonal time scales (not shown). On the other hand, as opposed to what was observed for SASS 30-90 (Fig. 5), no tropical wavenumber-1 structure is observed in the circulation anomalies associated with SASS 10-30 activity.

4. SASS Energetics

The previous analysis was complemented with an exploration of the energetics associated with the evolution of both SASS 10-30 and SASS 30-90. Two different parameters describing the eddy energy fluxes were considered in order to better understand the processes explaining the development of the large-scale circulation anomalies associated with SASS evolution: the wave activity fluxes (Plumb 1985) and the ageostrophic geopotential eddy fluxes (Orlanski and Katzfey 1991).

Wave activity flux (WAF) has been extensively used as diagnostic tool for the study of the 3D propagation of stationary waves. We considered the horizontal components of the fluxes as defined by Schubert and Park (1991), for cuasi-geostrophic stationary waves on a zonal mean flow:

$$F_\lambda = \frac{p}{2000a^2 cos\varphi}[\frac{\partial \psi'_r}{\partial \lambda}^2 - \psi'_r \frac{\partial^2 \psi'_r}{\partial \lambda^2}]$$

$$F_\varphi = \frac{p}{2000a^2}[\frac{\partial \psi'_r}{\partial \lambda}\frac{\partial \psi'_r}{\partial \varphi} - \psi'_r \frac{\partial^2 \psi'_r}{\partial \lambda \partial \varphi}]$$

where p stands for atmospheric pressure, φ for latitude, λ for longitude, a for the Earth's radius and ψ'_r are the temporal anomalies of the streamfunction previously regressed with the SASS index. WAF has proved to be useful in describing the source and propagation of Rossby waves (e.g.; Barlow et al. 2001; Brahmananda Rao et al. 2002). By design, WAF is parallel to wave group velocity and its divergence indicates the source regions for the perturbations. The meridional component, F_φ, depends on the momentum transport by the perturbations that is associated with the barotropic energy conversions. The zonal component, F_λ, is associated with the eddy horizontal structure. WAF were applied in the analysis of the perturbations presented in this work −even when they were strictly derived for stationary waves− under the assumption that the observed propagation speeds are very small.

The second methodology considered to describe eddy energy fluxes was the analysis of the ageostrophic geopotential eddy fluxes (e.g.; Chang and Orlanski 1994). Orlanski and Katzfey (1991) showed that when ageostrophic geopotential fluxes converge in a certain region, the creation of eddy kinetic energy is locally promoted. This mechanism frequently explains the generation of new perturbation centers downstream from the older centers, which radiate their energy through ageostrophic geopotential fluxes (e.g.; Orlanski and Katzfey 1991; Orlanski and Chang 1993; Chang 1993). In particular, Orlanski and Chang (1993) found that the downstream dispersion of wave energy via the ageostrophic geopotential fluxes was the triggering mechanism explaining downstream developing baroclinic waves over less baroclinic unstable regions. Furthermore, Chang and Orlanski (1994) showed that these energy fluxes are proportional to the group velocities of Rossby wave packets in baroclinic background flows.

This analysis is complemented with the evolution of the eddy kinetic energy (K_e), which was computed from the regressed vaues of both zonal and meridional winds at 200 hPa, onto the SASS indexes:

$$K_e = \frac{1}{2}[u'^2_r + v'^2_r]$$

where $'$ represents temporal anomalies and the subindex $_r$ implies that the regressed variables are considered. The ageostrophic geopotential fluxes play a role on the equation that describes the evolution of the eddy kinetic energy and therefore, a combined analysis of these parameters can help identify the processes that explain the observed evolution of circulation anomalies.

3.4.1 SASS 30-90

The WAF evolution associated with SASS 30-90 is presented in left column of Figure 11. Starting around day -25, at the beginning stages of the SASS negative phase, a divergence in the WAF is observed over New Zealand. During the following days, fluxes organize, evidencing an arch-shaped structure along the South Pacific. Between days -25 and -20 the first signs of inter-hemispheric energy propagation are observed in the tropical eastern Pacific and tropical western Atlantic, coinciding with the equatorial mean `westerly ducts' (not shown). By day -15, when the SASS negative phase is dissipating, it is possible to notice how the SACZ starts acting as a new wave source region, with fluxes that radiate towards the South Atlantic and reaching the Indian Ocean. Between days -15 and 0, fluxes are considerably strong over eastern SA, in association with the development of the SASS positive phase. Between days +5 and +10, the fluxes over SASS region weaken, coinciding with a new phase shift of the SASS. Furthermore, by day +10 a new WAF divergence region is observed over Australia and the fluxes progressively reorganize across the South Pacific, which is consistent with what was observed in Figure 4.

The evolution of the ageostrophic geopotential fluxes at 200 hPa was also analyzed for SASS 30-90 (Fig. 11b). Fluxes are significant in isolated and discontinuous regions, located between Ke centers (contours) and generally radiating downstream. Consistently with Figure 11a, the first days of the evolution reveal energy radiating from a convectively active region northeast of Australia (Fig. 3) and some inter-hemispheric propagation, particularly over the tropical Pacific is discernible. Between days -15 and -10, significant ageostrophic fluxes are observed over SESA, coinciding with a shift from the negative to the positive SASS phase. Subsequently, the SASS region starts acting as a wave source, with energy radiating towards the South Atlantic. Between days -10 and -5, the alternating areas with fluxes delimit an arch-shaped structure connecting the vicinity of New Zealand with SA, in agreement with the circulation anomalies in Fig. 5. The weakening of some centers, like the one located to the SE of Australia, is accompanied by the divergences of the ageostrophic flows. Between days +5 and +10, fluxes over the SASS region weaken, consistently with another phase shift.

4.2 SASS 10-30

WAF evolution for SASS 10-30 (Fig. 12a) presents the first significant signals between days -15 and -12, associated with zonally oriented fluxes starting at around $180°$ W and south of $40°$ S, along the southern branch of the westerly jet. Starting from day -9, when negative SASS phase settles, WAF intensifies over SA with a very strong SW-NE orientation.. An arch-shaped wave flux structure connecting the region to the SE of New Zealand with SA develops between days -6 and day +6. In particular, between days -3 and +3, a positive SASS phase progresses, while alternate centers of flux divergence and convergence propagate northeastwards over SA. Also, between days 0 and +3 part of the fluxes radiate towards the South Atlantic and converge over southern Africa. By days +3 and +6 large fluxes are observed along the Indian Ocean, and converging in the vicinity of Australia.

Figure 12b presents the evolution of the ageostrophic geopotential fluxes (vectors) and of K_e (contours). On day -15, the first significant fluxes are observed over the SW Pacific, in the proximities of New Zealand. Fluxes suggest that the observed wave trains originate from the westerlies channels near the date line. This feature allows to speculate that their generation is associated with changes in the divergence within the westerly jet (Weickmann 1983; Weickmann et al. 1985; Berbery and Nogues-Paegle 1992). Another notorious feature is the absence of K_e centers in the tropical band, near Africa and the Indian Ocean, that was previously linked for the 30-90 activity band with the tropical convective anomalies (Fig. 11a). From day -12, significant fluxes are observed in the proximities of southwestern SA, leading to the development of a negative SASS phase. They start being zonally-oriented but from day -9 onwards they acquire a SW-NE orientation and intensify notoriously. By that time, cross-equatorial propagation over the tropical Atlantic is discernible. Between days -3 and +3, a strong flux divergence stablishes over SESA simultaneously with a shift to the positive SASS phase. After day 0, as for WAF, the connection between the SASS region and the South Atlantic is evident. However, unlike what was found for SASS 30-90, no arch-shaped structure in the propagation over the South Pacific is observed by that time. The fluxes tend to be very weak in the western portion of the basin and to be zonally oriented in the south and southeast portions.

5. Summary and Discussion

This work explored the activity of the leading pattern of precipitation intraseasonal variability over SA –the SASS pattern– in its main activity bands: 30-90 days and 10-30 days. Two SASS patterns and their respective time series were obtained by performing two separate EOF analyses of the corresponding filtered OLR anomalies. It was found that for both bands of variability SASS is related to a dipole-like structure with OLR anomalies of opposite signs over the SESA and SACZ regions. For each SASS the large-scale features associated with the SASS activity were analyzed.

SASS activity in the 30-90 day band is characterized by a tropical dipole in convection that propagates to the east across the Indian and western Pacific Oceans. The associated circulation anomalies are characterized by a strong eastward propagating wavenumber-1 structure in the tropics. This observed evolution of both tropical convection and circulation anomalies is consistent with the life cycle of the MJO. In addition, the activity of the SASS 30-90 seems to be linked with tropical convection through Rossby-like wave trains with arch-shaped trajectories across the Southern Pacific ocean. The observed wave trains are equivalent barotropic and quasi-stationary.

On the other hand, the activity in the 10-30 day band does not seem to be connected with variations in the tropical convection. The evolution of the upper-level streamfunction regressions for the SASS 10-30 showed Rossby-like wave trains, as in the case of the 30-90 band, but that appear to originate in the subtropics, and not connected to significant convective anomalies. In addition, these waves showed larger propagation speeds that in the 30-90 case, though still weak. The fact that there are no clear subtropical convective sources for the observed wave trains does not necessarily imply that this mechanism is not present in this activity band. It might be the case that no clear source region can be detected due to the averaging procedure involved in the regressions calculation, combining cases with different source regions or triggering mechanisms

(Kiladis, personal communication). In addition, this higher frequency intraseasonal variability might be the result of modulations of synoptic-scale perturbations or of multi-scale interactions.

The study of the evolution of the eddy kinetic energy, along with the wave activity fluxes and the ageostrophic geopotential fluxes allowed to confirm that certain features of the observed wave activity, such as the presence of inter-hemispheric propagation and the arch-shaped patterns, can be explained by mechanisms such as barotropic energy conversion and downstream development of anomalous K_e centers.

In summary, this analysis allows to conclude that the SASS activity in the 30-90 band is strongly influenced by the MJO, through the excitation of Rossby-like wave trains in the tropics. In contrast, tropical convective activity does not seem to be involved in the triggering of SASS activity in the 10-30 day band. The latter seems to be linked to similar wave trains but that have subtropical sources, and could be related to changes in the properties of the westerly jet. A case study approach is proposed as an alternative method for exploring the large-scale features of this activity band, which could also inspire numerical simulations to complement the understanding of the dynamical mechanisms involved.

Finally, the evolutions of the OLR and streamfunction regressions suggest that there might be a significant interaction between the subtropical convergence zones (SPCZ, SACZ and SICZ) on intraseasonal timescales, as previously suggested by other authors (e.g.; Cook et al. 2004). Future studies will focus on better understanding these interactions as well as exploring how the large-scale features associated with both activity bands interfere constructively or destructively to determine the local SASS conditions.

5 Acknowledgements

This research was supported by UBACyT 20020100100434, and ANPCyT/PICT-2010-2110.

6 References

Barlow M, Nigam S, Berbery EH (2001) ENSO, Pacific decadal variability, and U.S. summertime precipitation, drought, and streamflow. J Climate, 14: 2105-2128.

Berbery EH, Nogues-Paegle J, Horel JD (1992) Wavelike Southern Hemisphere extratropical teleconnections. J Atmos Sci, 49:155-177.

Brahmananda Rao V, Chapa SR, Fernandez JPR, Franchito SH (2002) A diagnosis of rainfall over South America during the 1997/98 El Nino event. Part II: Roles of water vapor transport and stationary waves. J Climate, 15:513–522.

Bjornsson H, Venegas SA (1997) A manual for EOF and SVD analyses of climate data. CCGCR Rep. 97-1, McGill University, Montreal, QC, Canada, 52 pp.

Carvalho LMV, Jones C, Liebmann B (2004) The South Atlantic convergence zone: Intensity, form, persistence, and relationships with intraseasonal to interannual activity and extreme rainfall. J Climate, 17: 88-108.

Casarin DP, Kousky VE (1986) Anomalias de precipitacão no sul do Brasil e variacões na circulacão atmosférica. Rev Bras Meteorol , 1, 83-90.

Cavalcanti IFA, Castro CC (2003) Southern Hemisphere atmospheric low frequency variability in a GCM climate simulation. VII international Conference on Southern Hemisphere Meteorology and Oceanography, 24-28 March 2003, Wellington, New Zealand.

Cerne B, Vera C, Liebmann B (2007) The nature of a heat wave in eastern Argentina occurring during SALLJEX. Mon Wea Rev, 135:1165-1174.

Cerne B, Vera C (2011) Influence of the intraseasonal variability on heat waves in subtropical South America. Clim Dyn, 36: 2265-2277.

Chang EKM (1993) Downstream Development of Baroclinic Waves as Inferred from Regression Analysis. J Atmos Sci, 50:2038-2053.

Chang EKM, Orlanski I (1994) On Energy Flux and Group Velocity of Waves in Baroclinic Flows. J Atmos Sci, 51:3823-3828.

Cook KH (2000) The South Indian convergence zone and interannual rainfall variability over southern Africa. J Climate, 13:3789-3804.

Cook KH, Hsieh J, Hagos S (2004) The Africa–South America intercontinental teleconnection. J Climate, 17:2851-2865.

Cunningham CC, Cavalcanti IFA (2006) Intraseasonal modes of variability affecting the South Atlantic Convergence Zone. Int J Climatol. doi: 10.1002/joc.1309.

Diaz A, Aceituno P (2003) Atmospheric circulation anomalies during episodes of enhanced and reduced convective cloudiness over Uruguay. J Climate, 16:3171-3185.

Duchon CE (1979) Lanczos Filtering in One and Two Dimensions. J Appl Meteor, 18:1016-1022.

Ferranti L, Palmer TN, Molteni F, Klinker E (1990) Tropical-Extratropical Interaction Associated with the 30–60 Day Oscillation and Its Impact on Medium and Extended Range Prediction. J Atmos Sci, 47: 2177-2199.

Grimm AM, Silva Dias PL (1995) Analysis of tropical–extratropical interactions with influence functions of a barotropic model. J Atmos Sci, 52:3538-3555.

Gonzalez PLM, Vera CS, Liebmann B, Kiladis G (2008) Intraseasonal variability in subtropical South America as depicted by precipitation data. Clim Dyn, 30:727-744.

Hendon H, Salby M (1994) The life cycle of the Madden–Julian oscillation. J Atmos Sci,51: 2225-2237.

Jones C, Schemm J-K E (2000) The influence of intraseasonal variations on medium-range weather forecasts over South America. Mon Wea Rev, 128:486-494.

Kalnay E, Mo KC, Paegle J (1986) Large-amplitude, short-scale stationary Rossby waves in the southern hemisphere: Observations and mechanistic experiments to determine their origin. J Atmos Sci, 43:252-275.

Kalnay E et al. (1996) The NCEP/NCAR 40-Year Reanalysis Project. Bull Amer Meteor Soc, 77:437-471.

Li XL, Le Treut H (1999) Transient behavior of the meridional moisture transport across South America and its relation to atmospheric circulation patterns. Geophys Res Lett, 26, 10, 1409-1412.

Liebmann B, Smith CA (1996) Description of a Complete (Interpolated) Outgoing Longwave Radiation Dataset. Bull Am Meteor Soc, 77:1275-1277.

Liebmann B, Kiladis GN, Marengo JA, Ambrizzi T, Glick JD (1999) Submonthly convective variability over South America and the South Atlantic convergence zone. J Climate, 12:1877-1891.

Liebmann, B, Kiladis GN, Vera CS, Saulo AC, Carvalho LMV (2004) Subseasonal variations of rainfall in South America in the vicinity of the low-level jet east of the Andes and comparison to those in the South Atlantic convergence zone. J Climate, 17:3829-3842.

Lin JL et al. (2006) Tropical intraseasonal variability in 14 IPCC AR4 climate models. Part I: Convective signals. J Climate, 19:2665-2690.

Mo KC, Higgins RW (1998) The Pacific–South American Modes and Tropical Convection during the Southern Hemisphere Winter. Mon Wea Rev, 126:1581-1596.

Mo KC, Nogues-Paegle J (2001) The Pacific-South American modes and their downstream effects. Int. J of Climatol, 21:1211-1229.

Nogues-Paegle J, Mo KC (1997) Alternating wet and dry conditions over South America during summer. Mon Wea Rev, 125:279-291.

Nogues-Paegle J, Byerle LA, Mo KC (2000) Intraseasonal modulation of South American summer precipitation. Mon Wea Rev, 128: 837-850.

Orlanski I, Katzfey J (1991) The life cycle of a cyclone wave in the Southern Hemisphere. Part I: Eddy energy budget. J Atmos Sci, 48:1972-1998.

Orlanski I, Chang EKM (1993) Ageostrophic geopotential fluxes in downstream and upstream development of baroclinic waves. J Atmos Sci, 50:212-225.

Plumb RA (1985) On the three-dimensional propagation of stationary waves. J Atmos Sci, 42:217-229.

Sardeshmukh PD, Hoskins BJ (1988) The Generation of Global Rotational Flow by Steady Idealized Tropical Divergence. J Atmos Sci, 45:1228-1251.

Schubert SD, Park C-K (1991) Low-frequency intraseasonal tropical–extratropical interactions. J Atmos Sci, 48:629-650.

Slingo JM et al. (1996) Intraseasonal oscillations in 15 atmospheric general circulation models: Results from an AMIP diagnostic subproject. Clim Dyn 12: 325-357.

Vincent DG (1994) The south pacific convergence zone (SPCZ): a review. Mon Weath Rev, 122:1949-1970.

Waliser DE, Lau KM, Stern WF, Jones C (2003) Potential predictability and the Madden-Julian Oscillation. Bull Am Meteor Soc, 84: 33-50.

Weickmann KM (1983) Intraseasonal circulation and outgoing longwave radiation modes during Northern Hemisphere winter. Mon Wea Rev, 111:1838-1858.

Weickmann KM, Lussky GR, Kutzbach JE (1985) Intraseasonal (30–60 day) fluctuations of outgoing longwave radiation and 250 mb streamfunction during northern winter. Mon Wea Rev, 113:941-961.

Figure Captions

Figure 1: SASS pattern for the band: (a) 30-90 days, (b) 10-30 days, defined as the first EOF of filtered summer NOAA OLR for the period 1979-2007. The number between parenthesis indicates the amount of total FOLR variance explained by the pattern.

Figure 2: Power spectra of the SASS Index for the 10-30-days band (thick blue curve) and the 30-90-days band (thick red curve). The thin lines represent the null continuum, with respect to a red noise spectrum, and the 5% and 95% confidence levels.

Figure 3: Lagged regressions between the SASS 30-90 index and FOLR 10-90. Negative days indicate that FOLR is leading the evolution. Shaded colors are statistically significant at the 95% confidence level, according to a Student *t*-test. Contour interval is 1 W/m^2 and negative OLR anomalies (enhanced convection) is depicted in green.

Figure 4: Evolution of lagged regressions between the SASS 30-90 index and FOLR 10-90 in the centers of the dipole: 30° S 60° W (SESA center, green curve, full circles) and 10° S 50° W (SACZ center, black curve, open circles).

Figure 5: Lagged regressions between the SASS 30-90 index and zonal anomalies of streamfunction at $\sigma = 0.2101$. Negative days indicate that streamfunction is leading the evolution. Shaded colors are statistically significant at the 95% confidence level, according to a Student t-test. Contour interval is $5 \times 10^5\ m^2/s$.

Figure 6: Hovmöller diagram of lagged regressions between the SASS 30-90 index and zonal anomalies of streamfunction at $\sigma = 0.2101$ for the average of latitudes in the 20° S – Equator band. Shaded colors are statistically significant at the 95% confidence level, according to a Student *t*-test. Contour interval is $0.5 \times 10^6\ m^2/s$.

Figure 7: As Figure 3 but for the SASS 10-30.

Figure 8: As Figure 4 but for the SASS 10-30.

Figure 9: As Figure 5 but for the SASS 10-30.

Figure 10: Hovmöller diagram of lagged regressions between the SASS 30-90 index and zonal anomalies of streamfunction at $\sigma = 0.2101$ for the average of latitudes in the 60◦ S - 40◦ S band. Shaded colors are statistically significant at the 95% confidence level, according to a Student t-test. Contour interval is 0.5 $\times 10^6$ m^2/s.

Figure 11: Energetics of the 30-90 day band. The left panel presents the evolution of the wave activity fluxes obtained from the regressions with streamfunction at $\sigma = 0.2101$. The scale for the vectors is in the bottom right corner and the units are m^2/s^2. The shading describes the divergence of the fluxes and the units are m/s^2 . The right panel presents the ageostrophic geopotential fluxes obtained from the regressions with wind and geopotential heights at 200 hPa. The units are m^2/s. The contours present the evolution of the eddy kinetic energy constructed using the regressions between wind anomalies at 200 hPa and the SASS 30-90 Index. The contour interval is 0.5 m^2/s^2 . In all the panels the plotted values are statistically significant at the 95% level.

Figure 12: Same as Figure 11 but for the 10-30 day band.

Figures

Figure 1

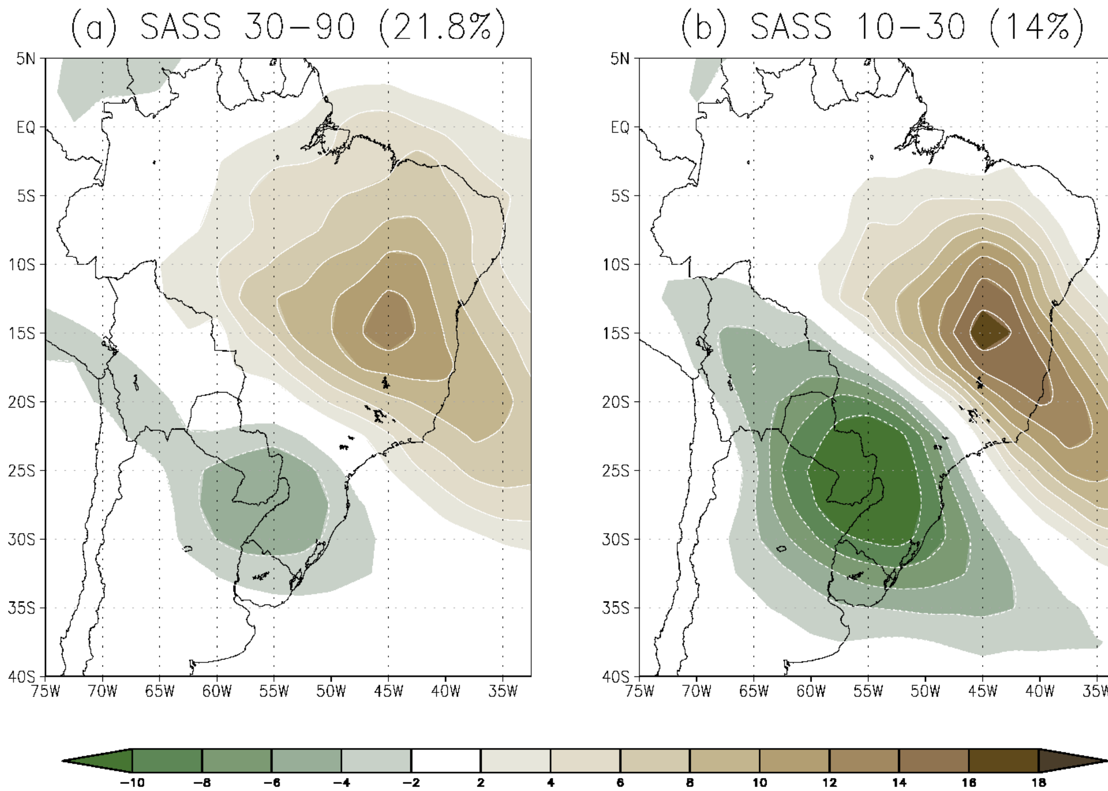

Figure 2

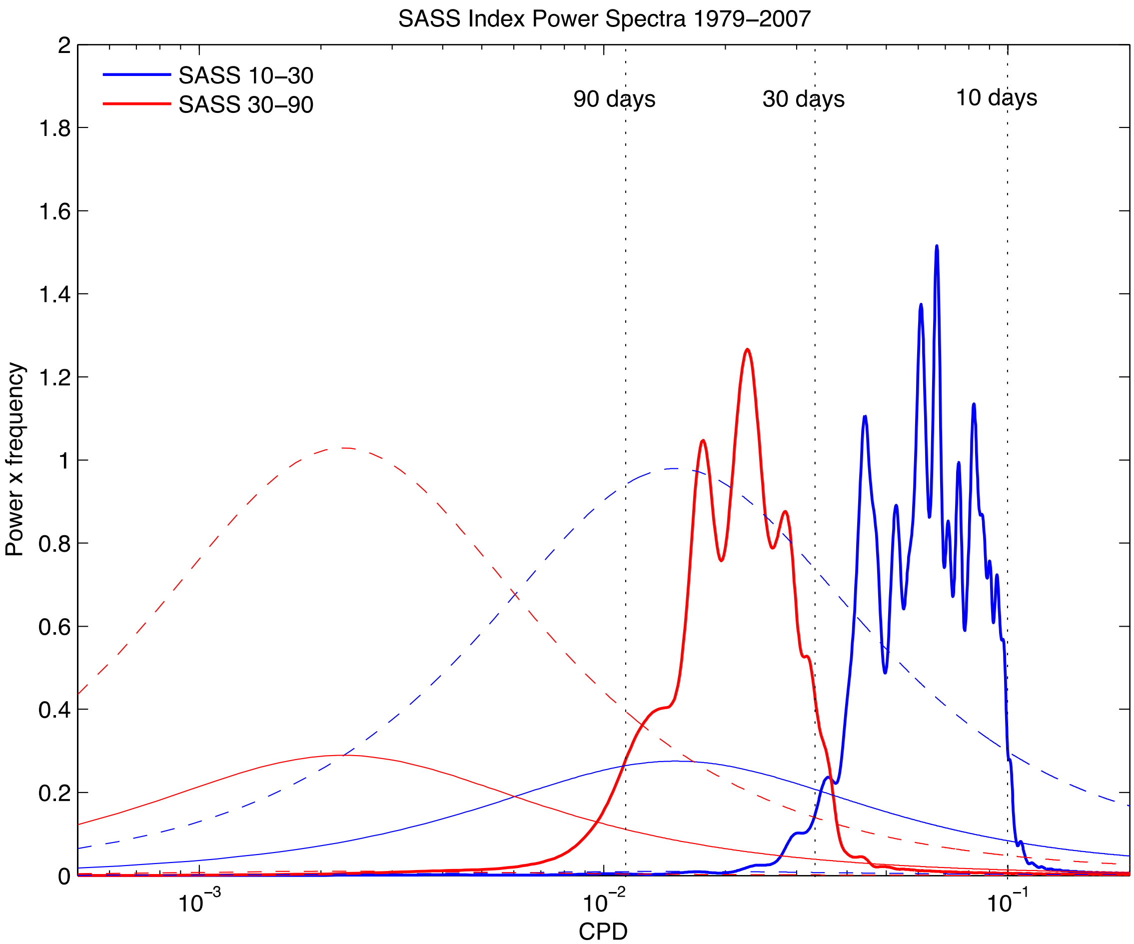
SASS Index Power Spectra 1979–2007
SASS 10–30
SASS 30–90
90 days
30 days
10 days
Power x frequency
CPD
0
0.2
0.4
0.6
0.8
1
1.2
1.4
1.6
1.8
2
10^{-3}
10^{-2}
10^{-1}

Figure 3

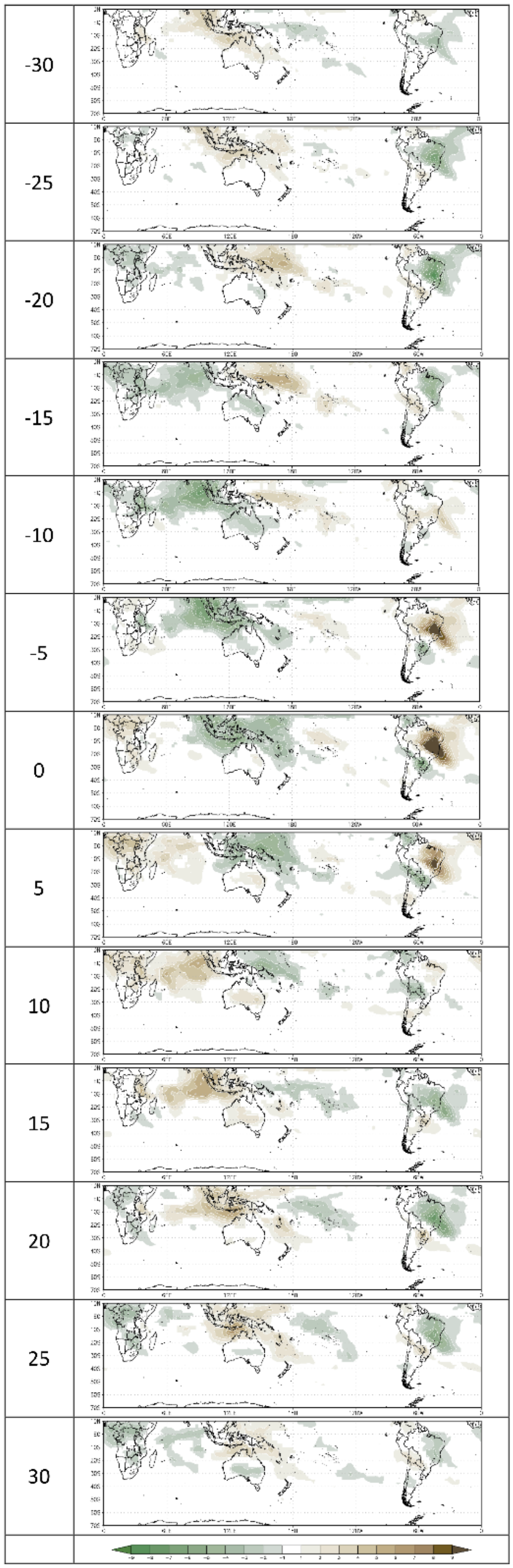

Figure 4

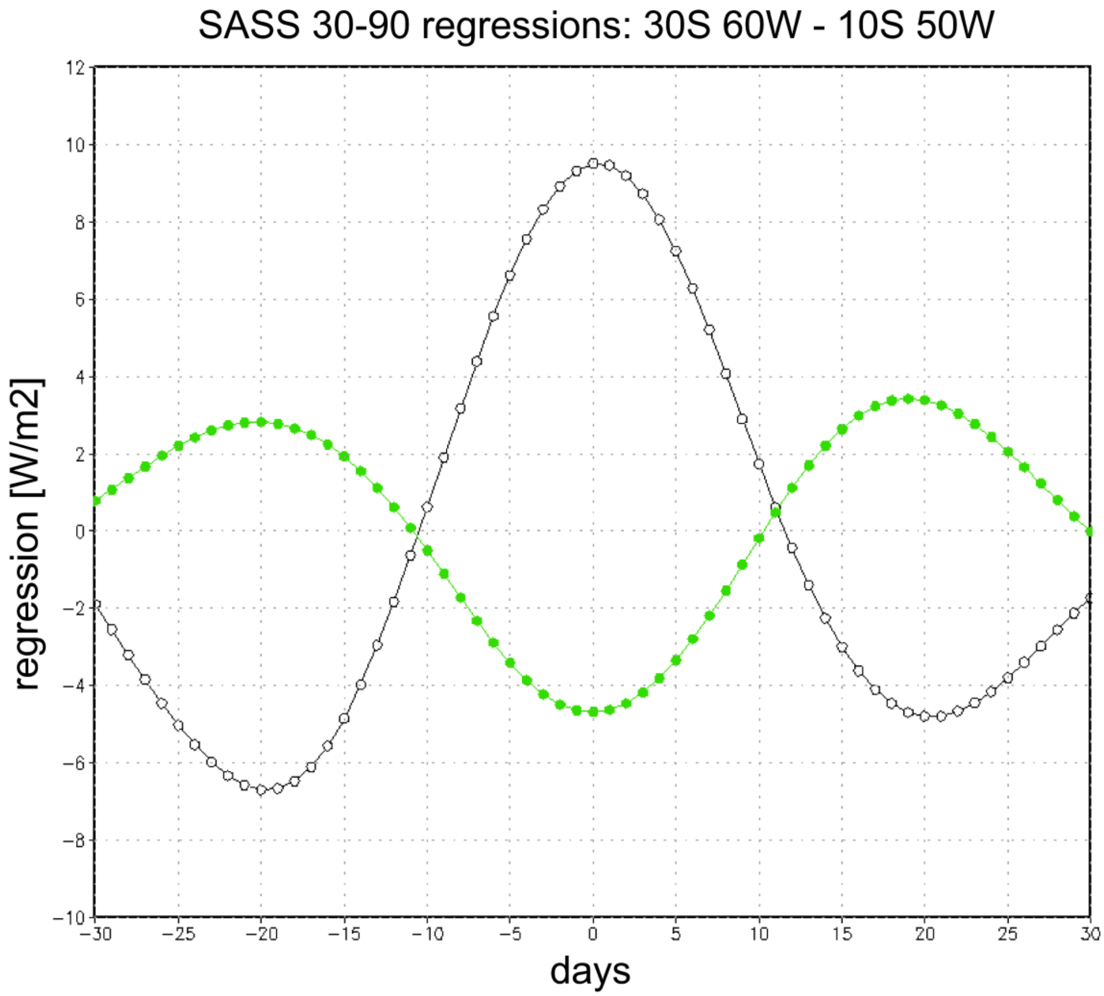
SASS 30-90 regressions: 30S 60W - 10S 50W
regression [W/m2]
days
12
10
8
6
4
2
0
−2
−4
−6
−8
−10
−30
−25
−20
−15
−10
−5
0
5
10
15
20
25
30

Figure 5

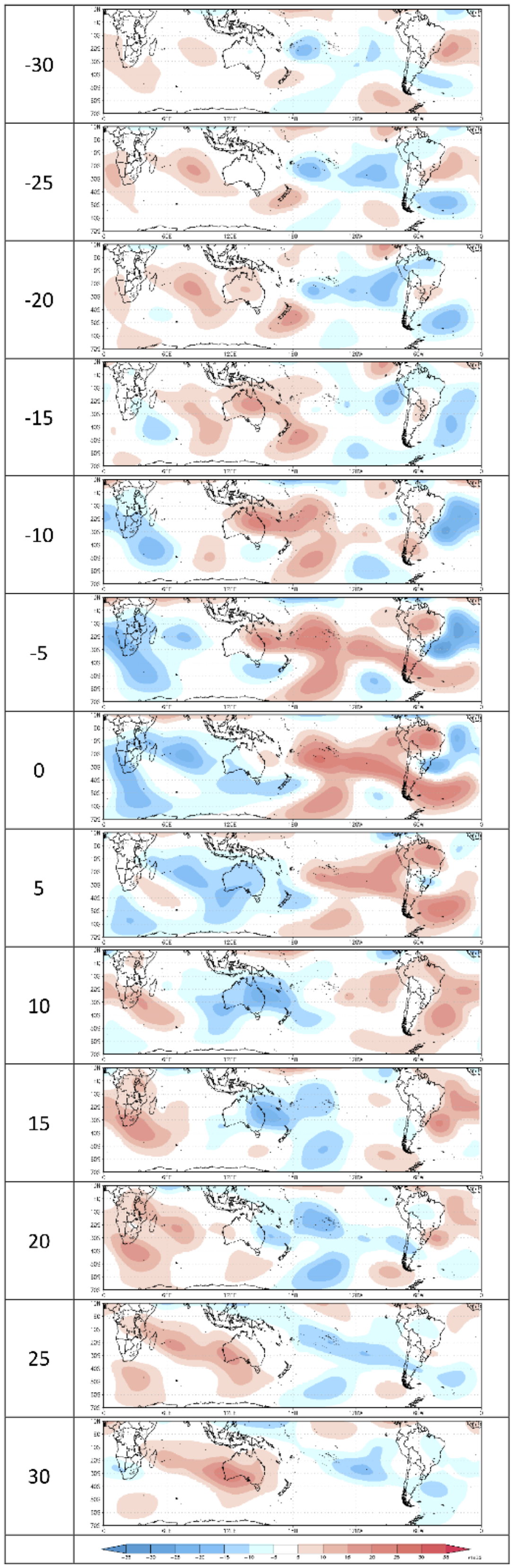

Figure 6

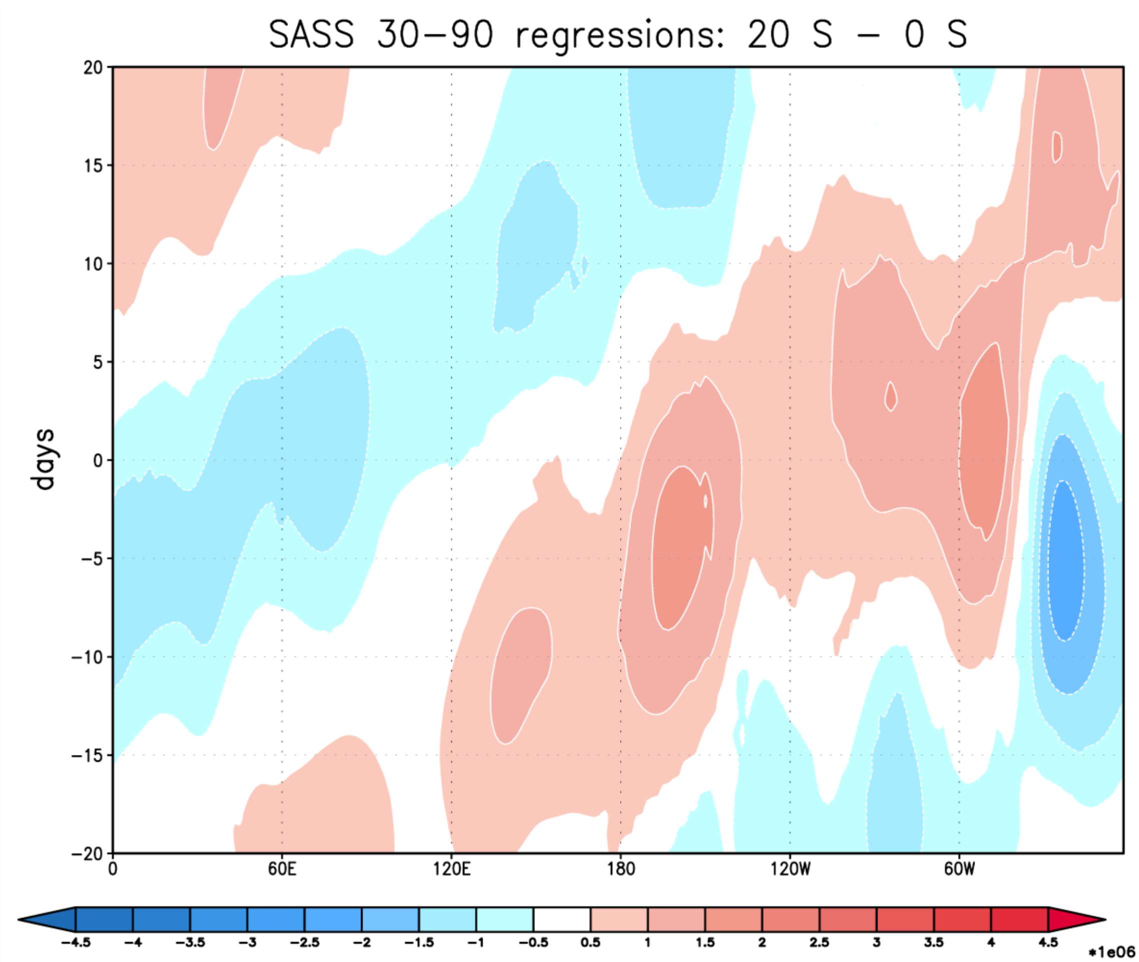
SASS 30−90 regressions: 20 S − 0 S
days
20
15
10
5
0
−5
−10
−15
−20
0
60E
120E
180
120W
60W
−4.5 −4 −3.5 −3 −2.5 −2 −1.5 −1 −0.5 0.5 1 1.5 2 2.5 3 3.5 4 4.5
*1e06

Figure 7

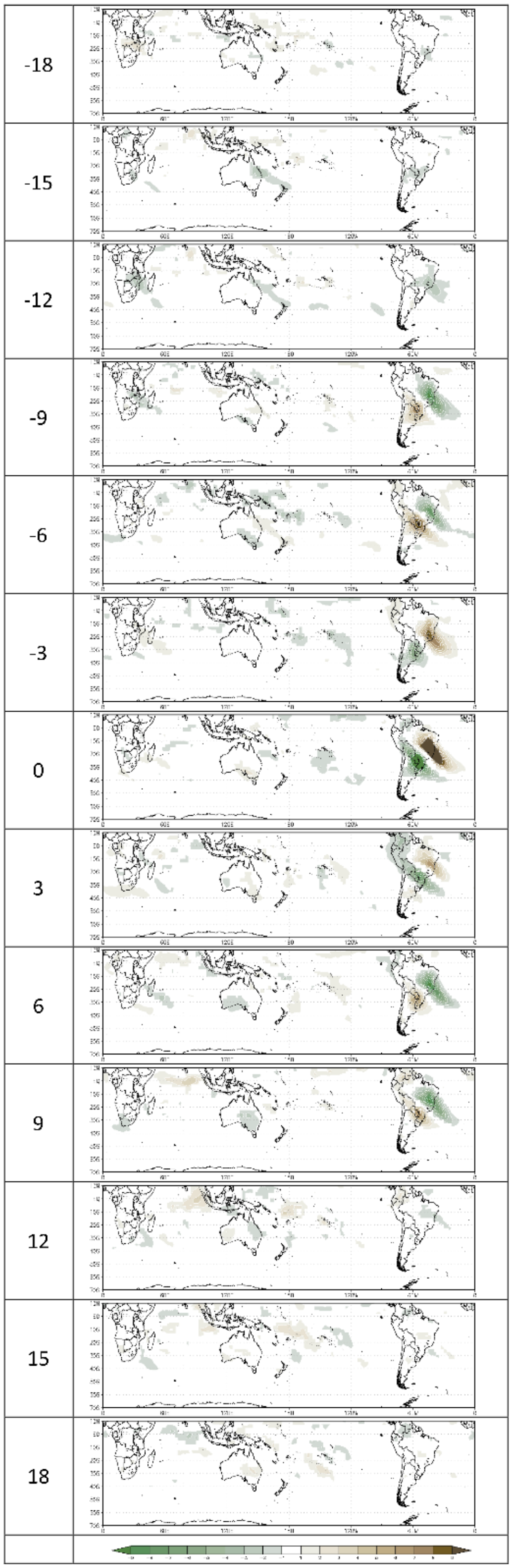

Figure 8

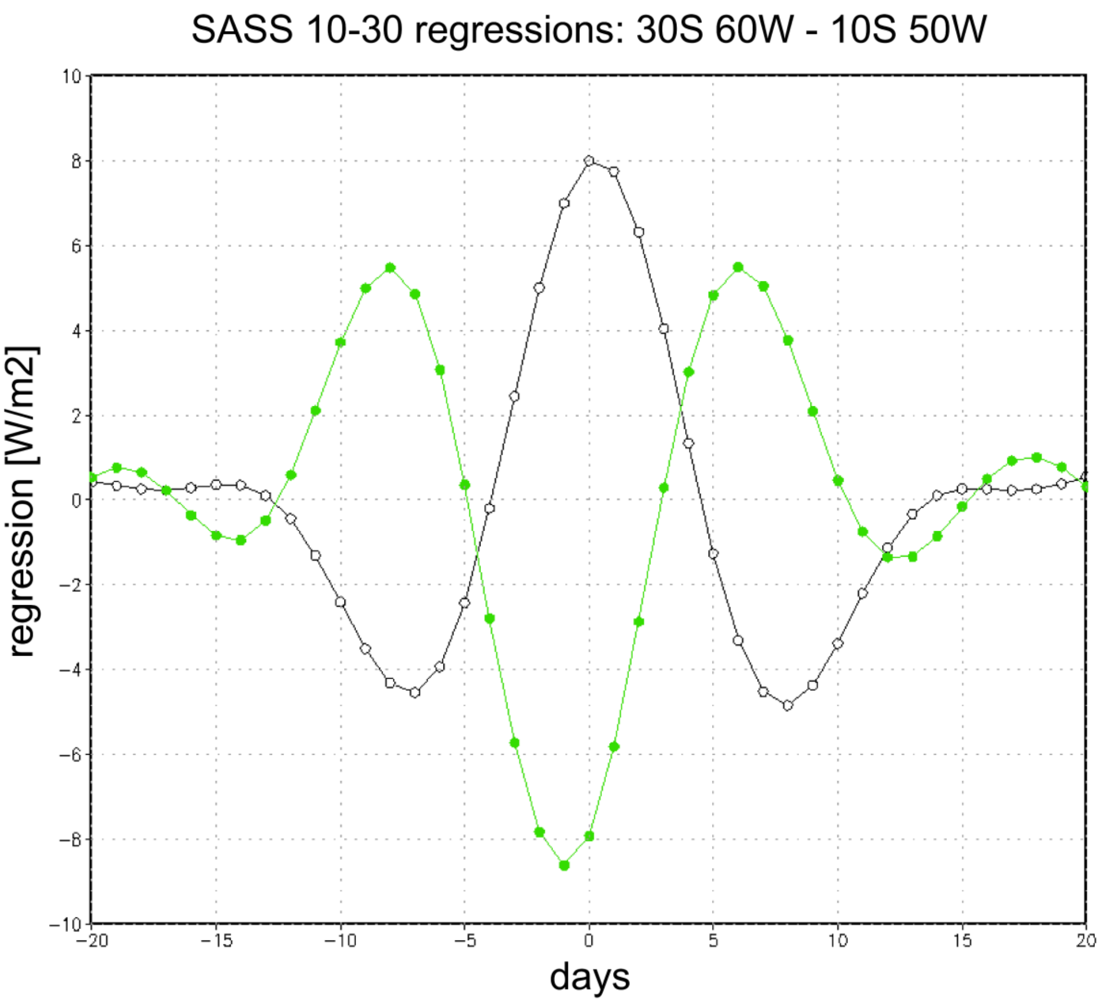
SASS 10-30 regressions: 30S 60W - 10S 50W
regression [W/m2]
days
10
8
6
4
2
0
−2
−4
−6
−8
−10
−20
−15
−10
−5
0
5
10
15
20

Figure 9

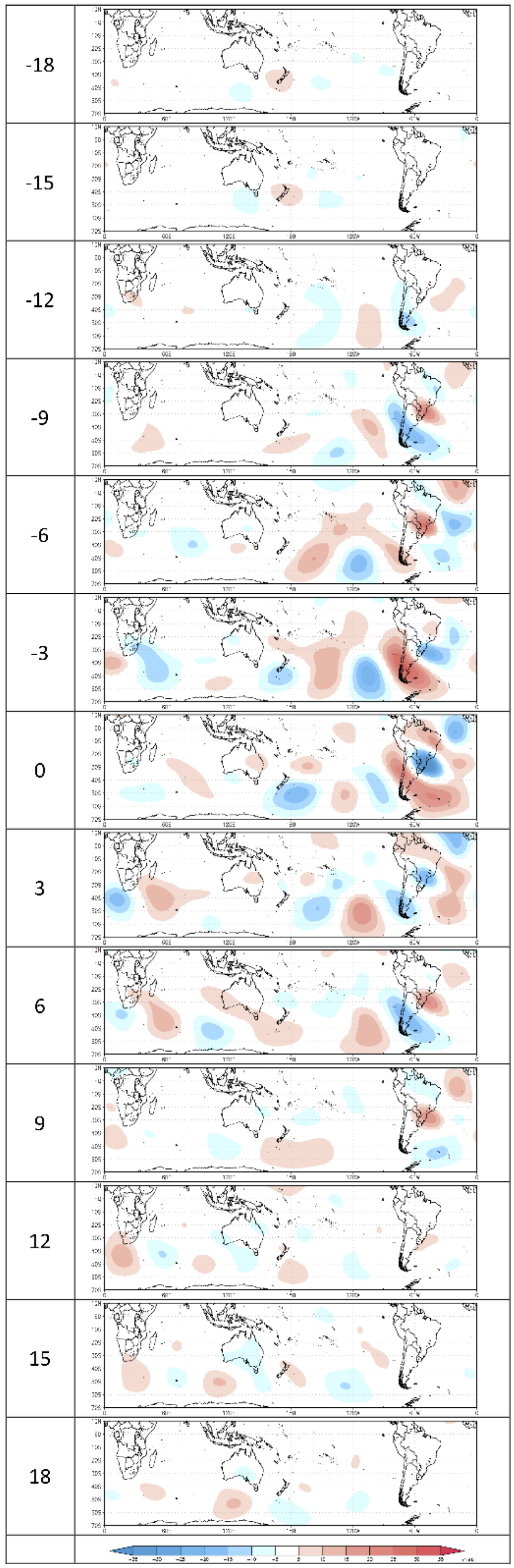

Figure 10

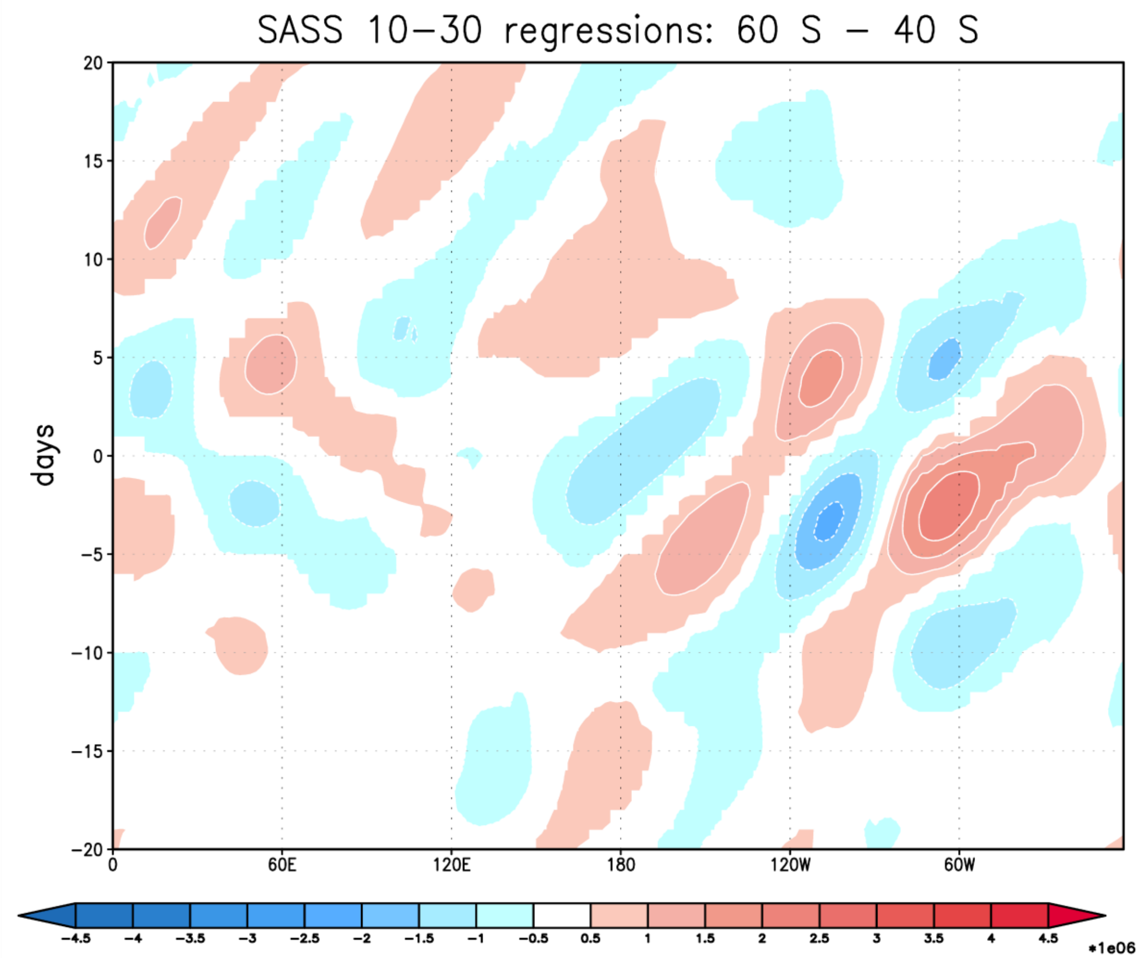
SASS 10−30 regressions: 60 S − 40 S
days
20
15
10
5
0
−5
−10
−15
−20
0
60E
120E
180
120W
60W
−4.5
−4
−3.5
−3
−2.5
−2
−1.5
−1
−0.5
0.5
1
1.5
2
2.5
3
3.5
4
4.5
*1e06

Figure 11

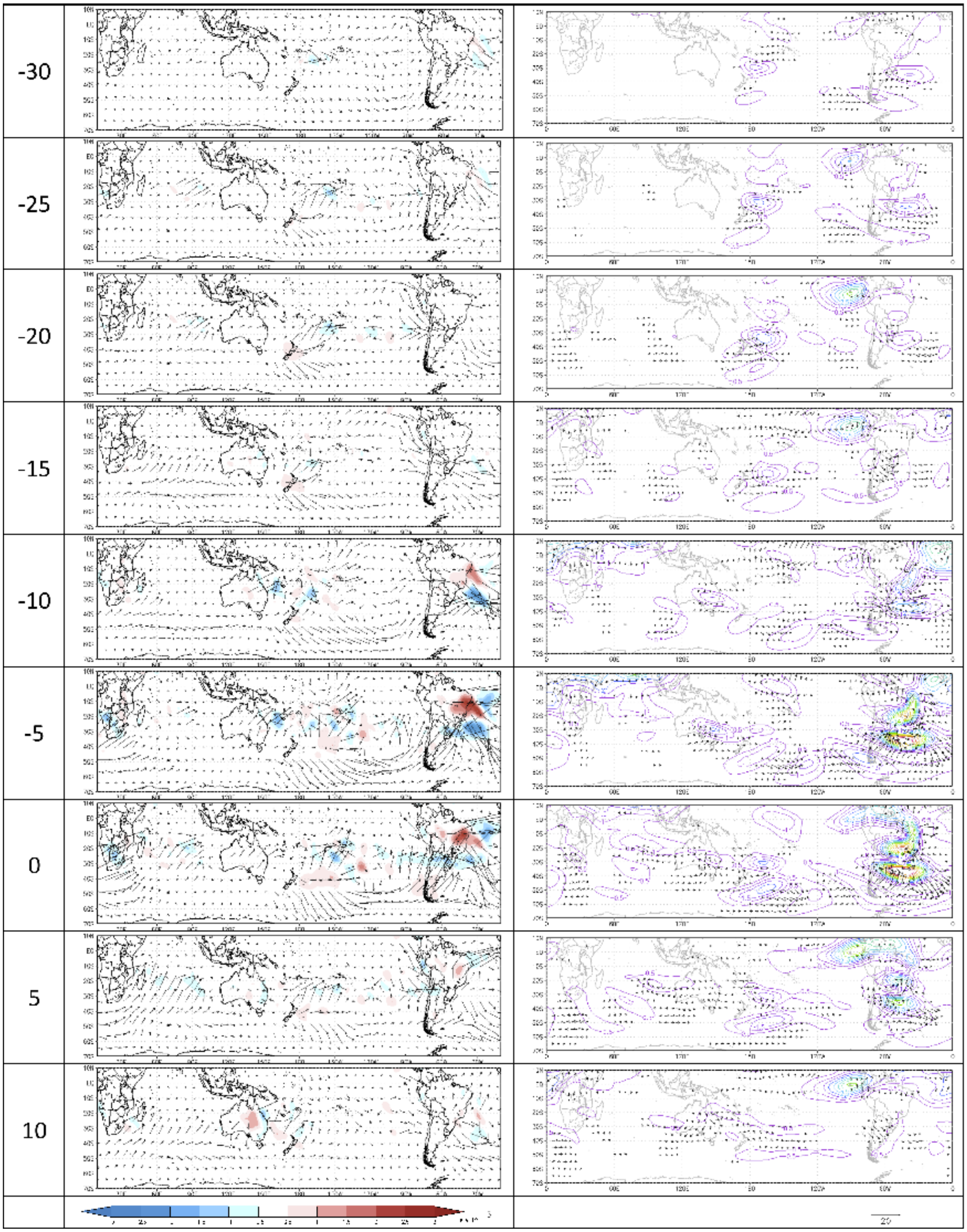

Figure 12